Journal Pre-proof

Comparison of highly conductive natural and synthetic graphites for electrodes in perovskite solar cells

Dmitry Bogachuk, Ryuki Tsuji, David Martineau, Stephanie Narbey, Jan P. Herterich, Lukas Wagner, Kumiko Suginuma, Seigo Ito, Andreas Hinsch

Please cite this article as: D. Bogachuk, R. Tsuji, D. Martineau, S. Narbey, J.P. Herterich, L. Wagner, K. Suginuma, S. Ito, A. Hinsch, Comparison of highly conductive natural and synthetic graphites for electrodes in perovskite solar cells, *Carbon*, https://doi.org/10.1016/j.carbon.2021.01.022.

This is a PDF file of an article that has undergone enhancements after acceptance, such as the addition of a cover page and metadata, and formatting for readability, but it is not yet the definitive version of record. This version will undergo additional copyediting, typesetting and review before it is published in its final form, but we are providing this version to give early visibility of the article. Please note that, during the production process, errors may be discovered which could affect the content, and all legal disclaimers that apply to the journal pertain.

Credit Author Statement

D.B. has generated the concept of this publication, coordinated the work, analyzed all the measurements and prepared the manuscript, as well as figures. R.T. and K.S. have provided the graphite powders, which were used to manufacture respective carbon-based pastes. R.T. has carried out the XRD measurements. D.B. has performed Raman spectroscopy. D.M. and S.N. have manufactured the carbon-based pastes, perovskite solution and complete PV-devices. D.M. has measured the sheet resistance of the carbon-based contacts by 4-point probe measurement and the J-V parameters of the manufactured solar cells. D.B. has carried out the EIS, SEM, optical microscopy, TRPL, V_{oc} decay and stability measurements. J.P.H. has performed a steady-state PL spectroscopy. L.W. and A.H. provided important conceptual ideas, contributed to the manuscript preparation and results interpretation. S.I. has provided essential ideas regarding the nature of graphite particles and differences in their properties. All authors have provided valuable comments to the manuscript.
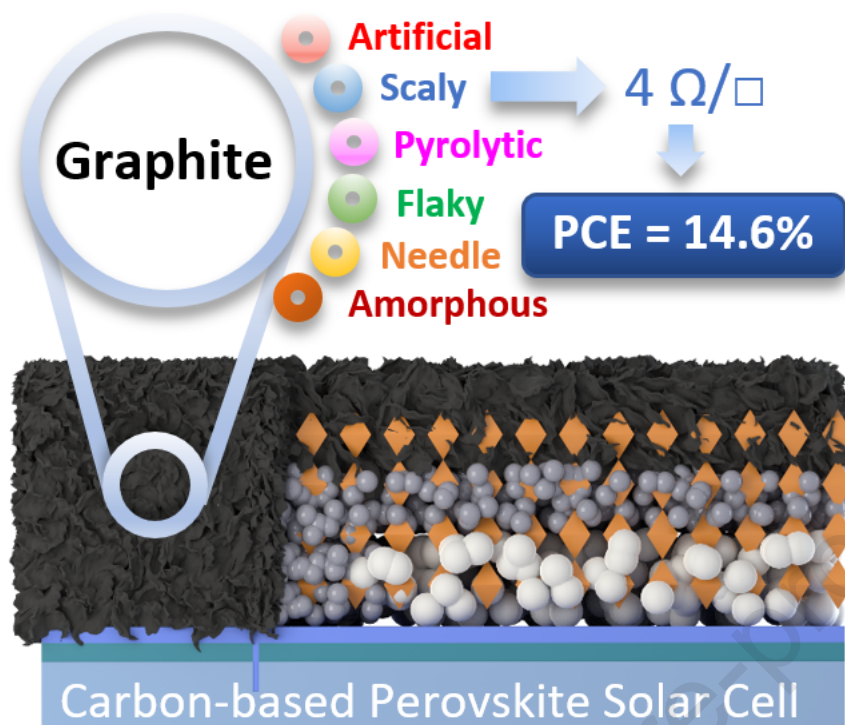
Comparison of highly conductive natural and synthetic graphites for electrodes in perovskite solar cells

Dmitry Bogachuk [ab*], Ryuki Tsuji [c], David Martineau [d], Stephanie Narbey [d], Jan P. Herterich [ae], Lukas Wagner [ab], Kumiko Suginuma [c], Seigo Ito [c] and Andreas Hinsch [a*]

[a] *Department of Organic and Perovskite Photovoltaics, Fraunhofer Institute for Solar Energy Systems ISE, Heidenhofstr. 2, 79110 Freiburg, Germany*

[b] *INATECH, Albert-Ludwigs-Universität Freiburg, Emmy-Noether-str. 2, 79110 Freiburg, Germany*

[c] *Department of Materials and Synchrotron Radiation Engineering, Graduate School of Engineering, University of Hyogo, 2167 Shosha, Himeji, Hyogo 671-2280, Japan*

[d] *Solaronix S.A., Rue de l'Ouriette 129, Aubonne 1170, Switzerland*

[e] *Materials Research Center FMF, Albert-Ludwigs-Universität Freiburg, Stefan-Maier-str. 21, 79104 Freiburg, Germany*

[*]*Corresponding authors:*
Tel: +4976145885587. E-mail: dmitry.bogachuk@ise.fraunhofer.de
Tel: +4976145885471. E-mail: andreas.hinsch@ise.fraunhofer.de

Abstract

In this work we compare seven different types of natural and synthetic graphite particles and examine how their integration into the cathode of carbon-based perovskite solar cells (C-PSCs) is influencing their opto-electronic properties. By combining x-ray diffraction, Raman spectroscopy and 4-point probe measurements we show that the differences in graphite crystallinity significantly affect the sheet resistance of the carbon-based cathode. The most conductive carbon-based film with an exceptional sheet resistance of 4 Ω/sq. have been produced from scaly graphite with the crystallite dimensions of L_a=60.6 nm and L_c=28.6 nm. Electrochemical Impedance Spectroscopy further revealed that charge transfer resistance at the perovskite/carbon contact differ for each graphite type. Overall, the pyrolytic graphite was found to be the best compromise between high conductivity and low charge transfer resistance leading to least series resistance losses and a fill factor (FF) above 74% (in perovskite solar cells with area of 0.64 cm^2). However, an overall efficient hole extraction and less non-radiative charge recombination in C-PSCs with scaly graphite resulted in the highest average power conversion efficiency and a champion device reaching 14.63%. All the C-PSCs display exceptional moisture stability for 5,000 h under ambient condition, with a PCE decrease of less than 3%.

Keywords: perovskite, graphite, photovoltaics, conductivity, carbon

1. Introduction

In recent years, the field of perovskite opto-electronic devices has attracted researchers across the globe due to the unique properties of perovskite materials, providing a broad spectrum of applications to explore.[1,2] One of the most rapidly developing fields is perovskite photovoltaics (PV), where the state-of-the-art laboratory-scale solar cells can already compete with the traditional silicon solar cells in terms of power conversion efficiency (PCE).[3] Despite tremendous progress in the development of strategies to boost PCEs of such solar cells, the up-scaling to perovskite solar modules is still challenging, partially due to the fact that most of the high-efficient devices have been manufactured by spin-coating method.[4,5] Additionally, the use of organic doped hole-selective layers (HSL) and costly counter electrodes, which consist of noble metals, not only strongly elevates the cost[6,7] and CO_2-footprint[8] of such PV devices, but also reduces their stability.[9–12] A solution to these issues can be realized by the implementation of the HSL-free perovskite solar cells with carbon-based electrodes (C-PSCs),[13] which primarily consist of graphite and carbon black particles.[14] These low-cost electrodes can provide a comparably high conductivity, while simultaneously hindering the moisture and air ingress into the PSC, owing to the hydrophobic nature of thick carbon-based back-contact.[15–18]

In 2014 Mei et al. have proposed to use a triple-layer C-PSC architecture consisting of mesoporous titanium dioxide (m-TiO_2) as electron-selective material, zirconium dioxide (ZrO_2), acting as a spacer layer and a carbon-based electrode, consisting primarily of graphite flakes and carbon black nanoparticles.[19] After the triple-layer m-TiO_2/ZrO_2/C cell stack is deposited, it is infiltrated with a perovskite precursor solution, which penetrates through the pores and crystallizes into perovskite photoabsorber upon the removal of the solvent (e.g. by annealing).[17,19–21] Although C-PSCs represent a promising route towards low-cost, stable and sustainable option for perovskite photovoltaics, the PCEs of those devices still lag behind the conventional ones with metallic electrodes and organic hole-selective layers.[22]

In C-PSCs, the graphite acts as both a hole extraction layer and a back-electrode. For the latter, it is important to achieve low series resistance losses to maximize the fill factor (FF), in order to reach high power conversion efficiencies in solar cells and modules. The total electrode resistance is defined by two parameters: material resistivity and electrode dimensions (i.e., width, length and thickness). As the width and length are determined by the layout, thickness can be

increased in order to reduce the series resistance. However, since in C-PSCs, the perovskite solution needs to penetrate through the entire porous cell stack, very thick electrodes result in incomplete pore filling and reduced photovoltaic performance. In addition to the lateral conductivity, the series resistance is also affected by the interfacial resistance that depends on the quality of the carbon/perovskite contact. Therefore, addressing the issue of electrode conductivity and interfacial resistance in C-PSCs becomes crucial for boosting the power conversion efficiencies (PCEs) of such cells.

Graphite is a crystalline material, consisting of hexagonally arranged 2D carbon sheets which are stacked onto each other via weak van der Waals interaction.[23] Over the years, the properties of different natural artificial graphite types have been studied by researchers in detail. However, a quantitative comparison of these graphite types in the context of applications for electrodes in perovskite solar cells has not yet been carried out and is therefore addressed here.

In this work, we demonstrate how the graphite crystal type which originates from the graphitization route influences the structural and electronic properties of the graphite particles and the carbon-based electrodes containing them, which consequently affect the performance of the final C-PSCs. The characteristics of six different types of graphite crystals have been investigated which will be referred to as artificial, scaly, pyrolytic, flaky, needle, amorphous graphites. These are compared with a reference graphite obtained from a commercially available carbon-graphite paste (Elocarb B/SP produced by Solaronix SA). Scaly (sometimes also referred to as lump or vein graphite), flaky and amorphous graphites belong to the naturally occurring types of graphite, which can be extracted from ore deposits. The high-quality artificial, needle and pyrolytic graphites are the so-called synthetic graphites, which can be produced from petroleum- or coal-based coke heated up to high temperatures (2500-3000°C) for graphitization – a process when carbon atoms re-arrange to form graphite particles.[24]

We have coupled the results from X-ray diffraction (XRD) with Raman spectroscopy to evaluate the crystallite dimensions and defect density of each graphite type. Each graphite type was furthermore used to produce separate carbon pastes, which were implemented to prepare carbon-based electrodes for the C-PSCs. We quantitatively compare the resistive losses due to different sheet resistance of these carbon-based electrodes. Moreover, the effect of the electrode on charge extraction and recombination at the carbon/perovskite interface were assessed to identify the

most optimal graphite type. The highest efficiency was achieved with a scaly graphite type electrode that yielded remarkably low sheet resistance of 4 Ohm/sq. and a PCE of 14.63% with a FF of 71.1% (on 0.64 cm²) These new findings highlight the significance of the choice of graphite for the development of efficient perovskite PV devices with carbon-based electrodes.

2. Experimental Details

2.1. Materials

Fluorine-doped tin oxide glass substrates TCO22-7/LI (sheet resistance 7 Ω/sq.), silver paste Elcosil SG/SP, titania paste Ti-nanoxide T165/SP, zirconia paste Zr-nanoxide ZT/SP, carbon-graphite paste Elocarb B/SP and methylammonium lead iodide perovskite solution with 5-ammonium valeric acid additive (5-AVAI) were provided by Solaronix SA. Acetone was purchased from Carl-Roth, ethanol was purchased from Alcosuisse. Titanium diisopropoxide bis (acetylacetonate) (75% in isopropanol), Hellmanex and isopropanol were purchased from Sigma-Aldrich. Flaky (V14), scaly (SPR150) and pyrolytic (PC30) graphite powders were obtained from Ito graphite Co. Amorphous and needle graphite powders were purchased from Oriental Industry Co. Ltd., whereas artificial graphite fine powders (UFG30) were purchased from Showa Denko K.K. Experimental graphite pastes were prepared as analogues of Elcocarb B/SP manufactured by Solaronix SA, substituting the reference graphite for another graphite types.

2.2. Fabrication of perovskite solar cells with carbon-based electrodes

Devices were fabricated on 10 x 10 cm² plates of FTO-coated glass. First, a laser pattern defined cathode and anode areas with an automated fiber laser. After that, the substrate was subjected to sequential cleaning steps in 1% aqueous solution of Hellmanex, acetone, and isopropanol respectively (15 min each) in an ultrasonic bath and subsequently dried in air. The thin compact titania layer (c-TiO$_2$) was grown by spray-pyrolysis on a hot-plate set to 450°C, using a glass mask to protect the contact areas. A volume of 20 mL of titanium diisopropoxide bis

(acetylacetonate) diluted in absolute ethanol (1:160) was sprayed with oxygen as a carrier gas, and warming was prolonged for 30 min before allowing the sample to cool down. An array of 18 electrodes was subsequently defined by screen-printing silver contacts, m-TiO$_2$, ZrO$_2$ and carbon paste using a 100-40, 165–30, 90–48, and 43–80 mesh stencil, respectively (the number of strands is per cm). After printing the wet film, each screen-printed layer was allowed to dwell for 10 min before drying at 120°C for 10 min, followed by a firing step at 500°C (or 400°C for carbon) for 30 min, after a 30 min ramp.

The freshly fired electrodes were masked with an adhesive polyimide gasket (provided by Solaronix) to delimit the wet area. The perovskite precursor was re-dissolved at 70°C right prior to use. An empirically determined volume of 5.76 µl of the perovskite precursor solution was dropped in the center of each electrode using a micropipette. The infiltration of the perovskite ink was done using a home-made semi-automated dispensing system. The wet samples were then moved to an oven set to 50°C where they were dried for 60 min, thus forming the perovskite crystals in the porous electrode structure. The polyimide adhesive gasket was carefully peeled off, and the solar cells were individualized by cutting the glass substrate into the corresponding solar cells. The resulting devices were submitted to heat and damp treatment at 40°C and 75%r.h. for 150 h. according to the previously reported method by Hashmi et al.[25]

2.3. Characterization

The crystal structure of the graphite was characterized by X-ray diffractometer MiniFlex II, Rigaku using CuKα radiation at a scan rate of 2°/min (for patterns between 3 and 0.4°/min (for more highly resolved patterns along specific planes). Raman spectra were measured on aWITec alpha500 Spectrometer with a Nd:YAG laser (λ = 532 nm) using a thermoelectrically cooled CCD detector in a range of 70-3700 cm^{-1}. The optical microscopy images were obtained by an OLYMPUS BX50 stereomicroscope and a sCMOS camera ("Zyla 5.5 sCMOS" by Andor) while the partial illumination of the sample was provided by a halogen lamp. To measure sheet resistance, a portion of the carbon paste was casted into a film on bare glass, which was covered on two ends with parallel strips of adhesive tape. Those acted as spacer for the subsequent blade-coating of the carbon paste. The freshly casted layer was fired at 400°C for 30 min. After cooling down to room-temperature, the sheet resistance of resulting carbon layer was measured in several places with a 4-pin probe sheet resistance meter Guardian Manufacturing SRM-232-100.

Scanning Electron Microscopy (SEM) images were obtained with a Zeiss Auriga 60 electron microscope. The current-density and voltage curves of as-prepared solar cells were measured under simulated AM1.5G illumination at a scan rate of 4.17 mV/s. Time-resolved PL decay measurement were conducted using an externally triggered, optically widened CW laser (Coherent Orbis) of 660 nm wavelength with 100mW power, with a fall and rise time (10% and 90%) below 2 ns. The laser was triggered to produce rectangular-shaped signals at 7Hz frequency. For the transient photovoltage measurement (V_{oc} decay), cells were illuminated using a red LED (635 nm) from Thorlabs. All the cells were light soaked for 15ms followed by switching off the light, after which the resulting voltage decay curve was captured using a PicoScope 5000 series. The measurement was carried out in a dark room to prevent the influence of stray light. The Electrochemical Impedance Spectroscopy (EIS) was carried out using a Ivium CompactStat in the frequency range of 100mHz to 1MHz at negative voltage bias and under illumination of 100 kLUX. Steady state Photoluminescence measurements were performed with an Andor Shamrock 193i Czerny-Turner type spectrometer. The illumination source is a frequency doubled Nd-YAG laser from Pegasus laser systems (Pluto, P532.400, λ=532 nm). Its intensity is adjusted to a value such that I_{SC} of the measured cell matches I_{SC} measured on the mismatch corrected solar simulator ensuring the PL measurement to be conducted in an excitation regime close to one sun illumination. The current-density and voltage curves of aged devices were measured with a source meter (Keithley 2400) at a scan rate of 50 mV/s using a class A solar simulator providing 100 mW/cm^2, AM 1.5G illumination.

3. Results and Discussion

The difference between various types of graphite crystals originates from the graphite formation process at the source (i.e. ore deposits) and/or preparation methods. These differences result in fundamentally different crystal structures and morphology, which have a direct impact on the electronic properties.[26] In this study, we compared six different types of graphite: artificial, scaly, pyrolytic, flaky, needle and amorphous. Additionally, the graphite used in the Elocarb B/SP carbon paste produced by Solaronix SA was considered as a reference, as it is often used for the preparation of C-PSCs.[21,25,27–29]

We firstly perform X-ray diffraction measurement on graphite powders, in order to gain insights into the graphite crystal structure. Since graphite is a polycrystalline material, one needs to

differentiate between the flake/particle (which is normally in the µm range) and the crystallite size, which consists (with exceptions of impurities) of periodically repeated and hexagonally arranged carbon atoms. Fig 1a, displays a visual representation of a small graphite particle/flake consisting of four crystallites as an example. From the XRD patterns of each graphite type (Fig. 1b) the most pronounced peak appears at approximately $2\theta = 26.4°$, corresponding to the (002) plane (Fig. 1b). Additionally, peaks at $2\theta = 44.1\text{-}44.5°$, $42.1\text{-}42.3°$, $54.4\text{-}54.5°$, $59,5°$ and $77.1\text{-}77.4°$ corresponding to (100), (101), (004), (103) and (110) planes, respectively, can be observed.
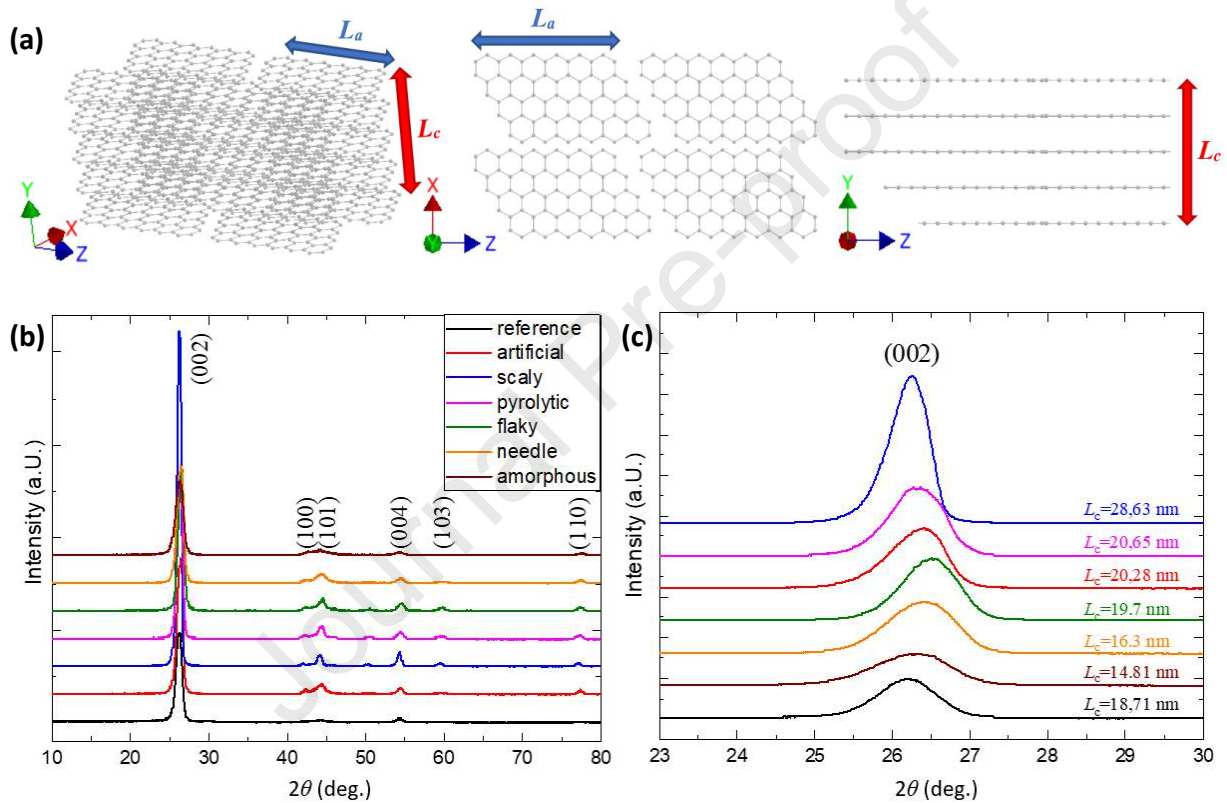

Figure 1: *(a) Illustration of a graphite particle consisting of crystallites, represented by stacked uninterrupted 2D carbon layers, depicting crystallite height (L$_c$) and lateral dimensions (L$_a$) (b) XRD patterns of different types of graphites, showing reflections affiliated with corresponding planes. (c) close-up of image a), showing diffraction intensities of different types of graphite along (002) plane.*

The diffraction intensity along such (00l) planes can be related to the crystallite height (L$_c$),[30–32] whereas intensities from (hk0) planes yield information about the size of a 2D carbon layer (L$_a$),[30,33,34] illustration of which can be seen in Fig. 1c. We use Scherrer equation with a shape factor $K = 0.94$ for polycrystalline graphite to find the crystallite height from the diffraction along (002) plane, revealing that the scaly graphite has the highest L$_c$ of 60.6 nm, followed by artificial (51.5 nm), pyrolytic (50.3 nm) and flaky (48.3 nm) graphites, while amorphous, needle

and our reference graphite exhibit lower crystallite height. The two-dimensional carbon layer dimensions L_a, determined from the (110) reflection, can be derived, according to Warren,[33] by:

$$L_a = \frac{1.84 \cdot \lambda}{FWHM \cdot \cos\theta}$$

The calculated L_a for different types of graphites are displayed in Table 1, where the scaly graphite has the largest crystallite lateral size of 28.6 nm. These results show that after the graphitization process, scaly graphite provides the largest crystallites (regarding height and lateral size). We hypothesize that graphites with a larger uninterrupted periodic crystal structure would result in less grain boundaries and provide better charge carrier mobility as well as faster charge transport along graphite, resulting in better conductivity.

Table 1: *Crystallite height (L_c), crystallite lateral dimensions (L_a) and I_D/I_G band ratio describing the lattice disorder in different types of graphites.*

Graphite type	L_c (nm)	L_a (nm)	I_D/I_G
Reference	18.7	43.7	0.08
Artificial	20.3	51.5	0.069
Scaly	28.6	60.6	0.064
Pyrolytic	20.7	50.3	0.033
Flaky	19.7	48.3	0.041
Needle	16.3	42	0.113
Amorphous	14.8	37.8	0.109

To gain more insight into the density of crystal defects, Raman spectra of each graphite type were measured (Fig.2). The bands at 1355 cm^{-1} and 1580 cm^{-1} are commonly attributed to D and G bands respectively, while the 2D band appears at around 2670 cm^{-1}. The D band is normally defect-induced and occurs only when the translational symmetry of two-dimensional carbon periodic structure is broken, resulting in A_{1g} vibrational mode, while the G band is strongly related to the E_{2g} vibrational mode of the sp^2-hybridized carbon lattice.[30,34] Therefore, the intensity ratio of D and G bands (I_D/I_G) is often used as a measure of lattice disorder,[34,35] which is low for highly crystalline graphene/graphite and high for turbostratic or disordered structure of non-graphitic carbon. As seen from the obtained Raman shift spectra in Fig. 2, the I_D/I_G is increasing in the order pyrolytic < flaky < scaly < artificial < reference < amorphous < needle. This result suggests that pyrolytic type of graphite possesses the lowest number of structural defects and provides potential for reaching higher charge carrier mobility and layer conductivity,

consistent with the demonstrated reports displaying well-aligned individual crystallites with a low mosaic spread angle in pyrolytic graphite.[36]
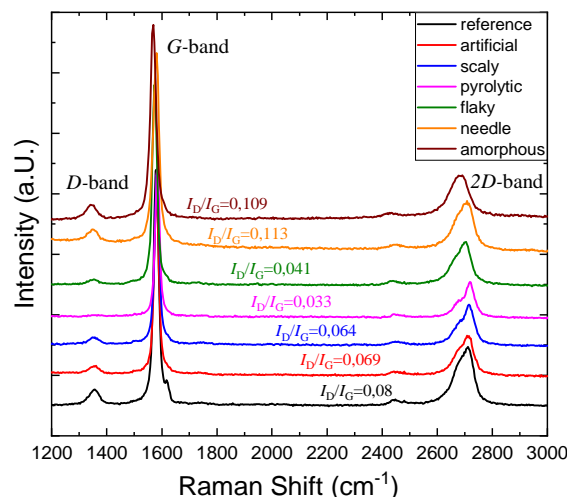

Figure 2: Raman shift spectra of different graphite types, highlighting the D-, G- and 2D-bands, as well as the ratio of intensities of D- and G-bands for each type.

Coming from the sub-nanometer crystallites to the larger graphite flakes, we recorded SEM images, of powders of each graphite type, as presented in Figs. S1 and S2. The flakes of artificial, scaly, pyrolytic and flaky tend to be larger and more parallel-stacked, whereas the amorphous one tends to form separate small-sized clusters. Our reference graphite does not exhibit large crystals, although tightly interconnected in between and seems to be more truncated than most of other graphite types.

Next, these graphite powders were used for the preparation of respective carbon-based pastes, in order to screen-print them on the cell stack shown in Fig. 3. The pastes were prepared in exactly same manner as it was done for the reference Elocarb B/SP paste, except for the replacement of reference graphite with the natural and synthetic graphite powders described above. Regarding the optical appearance, the pastes with needle and amorphous types proved to result in layers of comparable high quality as homogeneously as the reference one. In contrast, those containing artificial and flaky graphites seemed to be printed less homogeneous, as seen from the optical microscopy images in Fig. S3 where an obvious pattern resulting from the screen mesh is visible. Moreover, in all the deposited layers, except for the reference and the one containing pyrolytic graphite, several small voids could be observed in the microscope, possibly arising from the

inhomogeneous spreading of the paste. The pastes containing scaly graphite was the most challenging to print evenly across the whole printing pattern, suggesting a correlation between the graphite flake size and paste rheology.
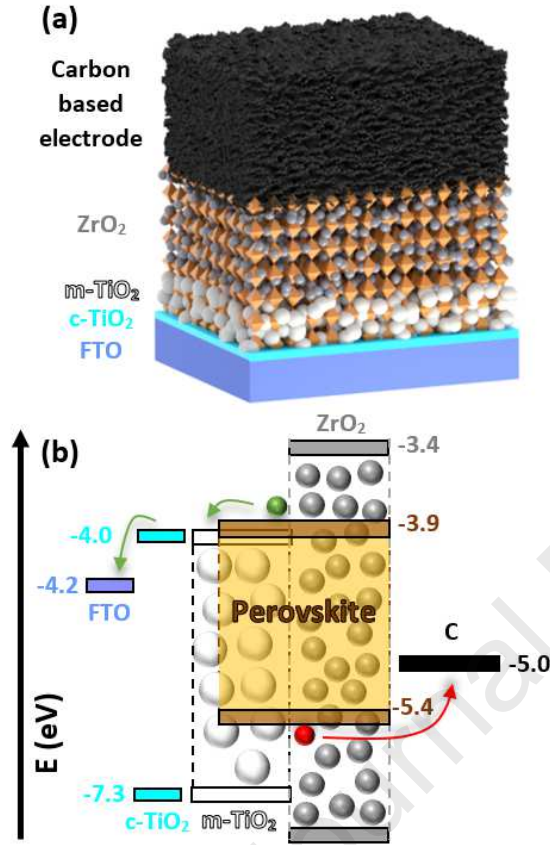

Figure 3: (a) Architecture of the fabricated carbon-based perovskite solar cells. (b) Energy band diagram of the C-PSCs depicting the extraction of photogenerated electrons (green) and holes (red) by the m-TiO$_2$ and carbon-based electrode, respectively.

The fabricated C-PSCs have a standard structure , constituting fluorine-doped tin oxide (FTO) as a front electrode, compact titanium dioxide (c-TiO$_2$) as a hole blocking layer, mesoporous titanium dioxide (m-TiO$_2$) acting as an electron selective layer, a spacer layer of zirconium dioxide (ZrO$_2$) covered by a carbon-based back-electrode (Fig.3). After the cathode deposition, the cells were filled with the mixed dimensional (2D/3D) $5AVA_{1-x}(CH_3NH_3)_xPbI_3$ perovskite absorber, employing an automatic CNC-controlled pipetting device with precisely controlled drop-casting. The measured photoluminescence (PL) spectra of each cell type (Fig. S4) confirmed the peak position at 764 nm and a bandgap of 1.62 eV, consistent with the previous reports on C-PSCs with such absorber.[27] Since the perovskite properties are not influenced by the

graphite type in the electrode, it is not surprising that the PL peak for all cell types is the same. Nine cells with carbon-based electrodes of each graphite type were fabricated and J-V scans were measured under a solar simulator. The current density (J_{sc}), open-circuit voltage (V_{oc}), fill factor (FF) and power-conversion efficiency (PCE) are presented in Fig. 4. Cells with reference, artificial and scaly graphites display slightly higher J_{sc} and V_{oc} than the pyrolytic, flaky and needle graphites. The most pronounced difference between the cells is seen in the FF. This is not surprising, considering that one of the main roles of carbon-based layer is being a back-contact of the cell and the resistance losses in the cell are strongly affected by it. Remarkably, some C-PSCs with electrodes constituting pyrolytic graphite flakes have FFs even above 74%, although the devices with scaly and artificial graphites that yielded the highest PCE did not have the highest FFs. The scaly graphite in the carbon-based electrode was found to be the most optimal type, leading to a champion efficiency of 14.63%. Notably, as seen from the cross-sectional SEM (Fig S5) images although the carbon-based electrodes with scaly graphite were found to be the thinnest (probably attributed to inhomogeneous layer printing), their sheet resistance is the lowest, suggesting that the FF can be further improved by increasing the electrode thickness.
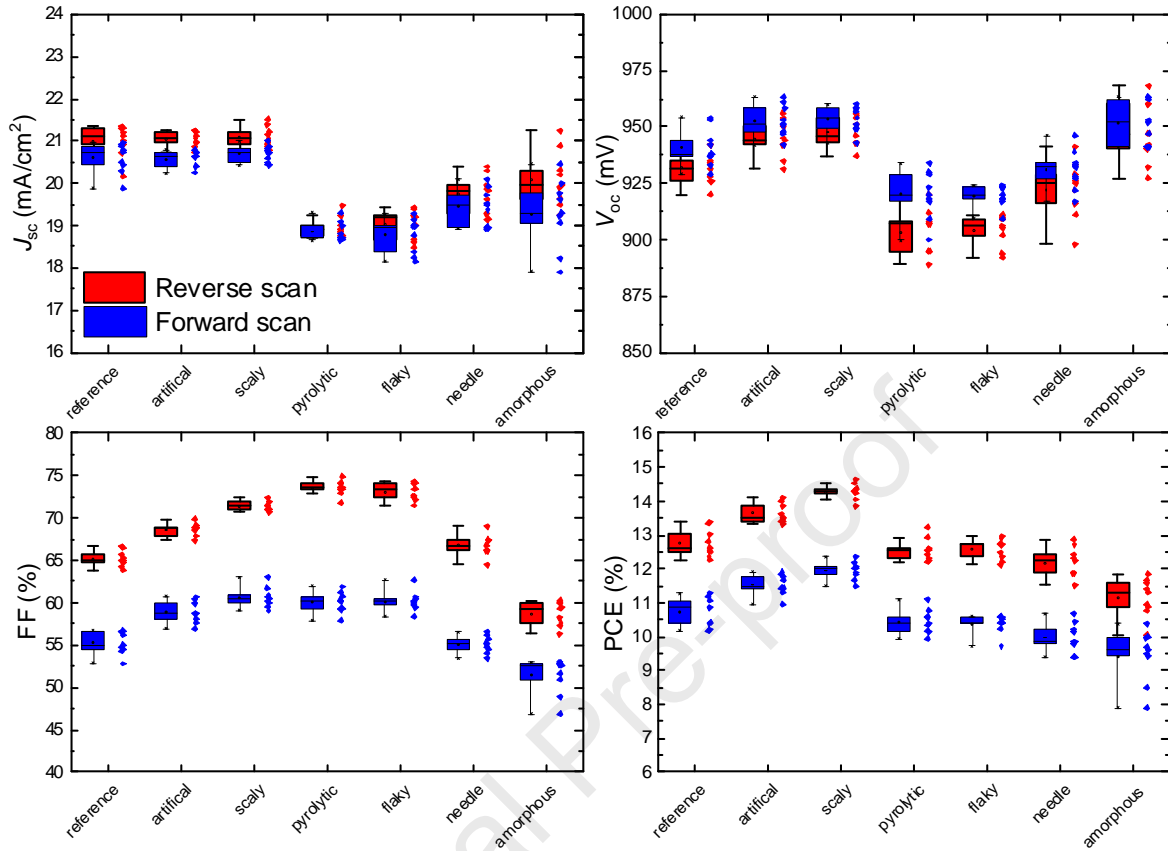
Figure 4: *JV-parameters obtained from reverse (red) and forward (blue) voltage sweeps of C-PSCs with electrodes made of different graphite types.*

To elucidate the influence of graphite type on the cell's series resistance losses we performed sheet-resistance measurement and electrochemical impedance spectroscopy (EIS) on the cells. From the sheet resistance measurement shown in Fig. 5, the scaly and pyrolytic graphites display exceptionally low sheet resistance close to 4 Ω/sq. lower than the sheet resistance of conducting oxides such as fluorine- or indium-doped tin oxides with comparable sheet resistances of 7-10 Ω/sq. and 13-20 Ω/sq. respectively,[37–39] which are widely used in PSCs. Moreover, all the other types of carbon-layers except for needle, reference and amorphous ones, exhibit sheet resistance below 10 Ω/sq. highlighting great potential to be an efficient alternative to costly metal-based contacts. From Fig. 5 it can be seen that the trends between the sheet resistance and the series resistance (R_s) extracted from the EIS measurements are in good accordance. The results indicate that the high crystallite height L_c, low number of structural defects, high graphite crystallinity and flake stacking (as in the case of scaly, artificial, pyrolytic and flaky graphites) seem to strongly reduce the series resistance losses of the solar cell, positively influencing the PCE.
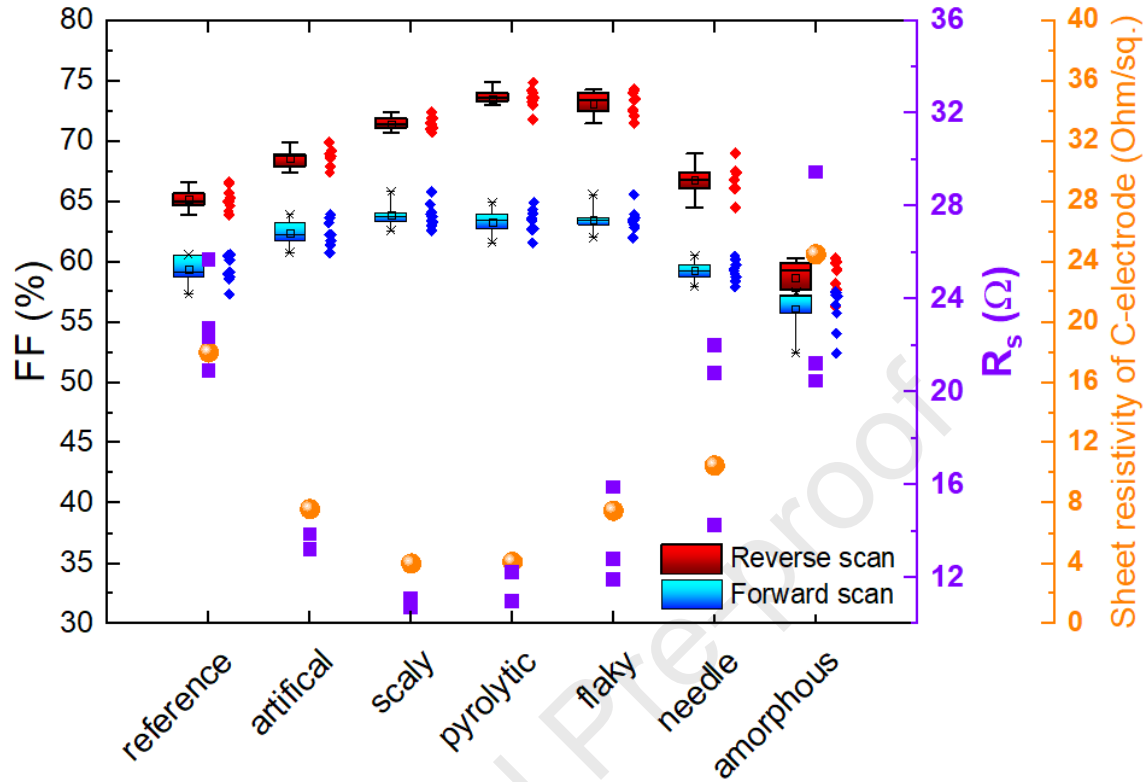
Figure 5: Fill factor of C-PSCs fabricated using different graphite sources from applied reverse and forward voltage scans, which correlates with the sheet resistance of the respective carbon-based electrode and series resistance (R_s) obtained from the Nyquist plot (3 cells per group are shown, measured at 0.6V).

Looking at the SEM cross-section of the cells, presented in Fig. S5, we note that the cells with artificial, scaly, pyrolytic and flaky graphites are well-aligned along the longitudinal plane (i.e. in-plane with the substrate) providing an efficient lateral charge transport through the highly conductive carbon-based contact. On the contrary, in needle graphite vertically arranged flakes are frequently occurring, hindering efficient charge transport along the longitudinal plane. In amorphous layers, the graphite flakes are much smaller than in other cells. This indicates that the exceptionally low series resistance of the cells with scaly, pyrolytic and flaky graphites could also partially originate from the large and well-aligned flakes of the respective carbon layers.

Although the correlation between the R_s of the cell and FF are clear, there are some deviations from this trend (e.g. the most conductive scaly graphite does not have the highest FF). At the Nyquist plot in Fig.S6, two semicircles can be observed: the high-frequency one, which was attributed to the perovskite/carbon interface and the low-frequency one, which corresponds to

charge recombination resistance at perovskite/TiO$_2$ interface. The latter one is similar in all cells regardless of the respective graphite type due to unaltered properties of the perovskite/TiO$_2$ contact. The perovskite/carbon interface changes depending on the graphite type in the carbon-based electrode. As shown in Fig.6b, the lowest interfacial resistance (R_{CE}) at the counter-electrode was seen in the flaky graphite, followed by the artificial one. Therefore, we postulate that the FF is influenced by the final interplay between the R_s and the interfacial resistance R_{CE} at the perovskite/carbon contact.
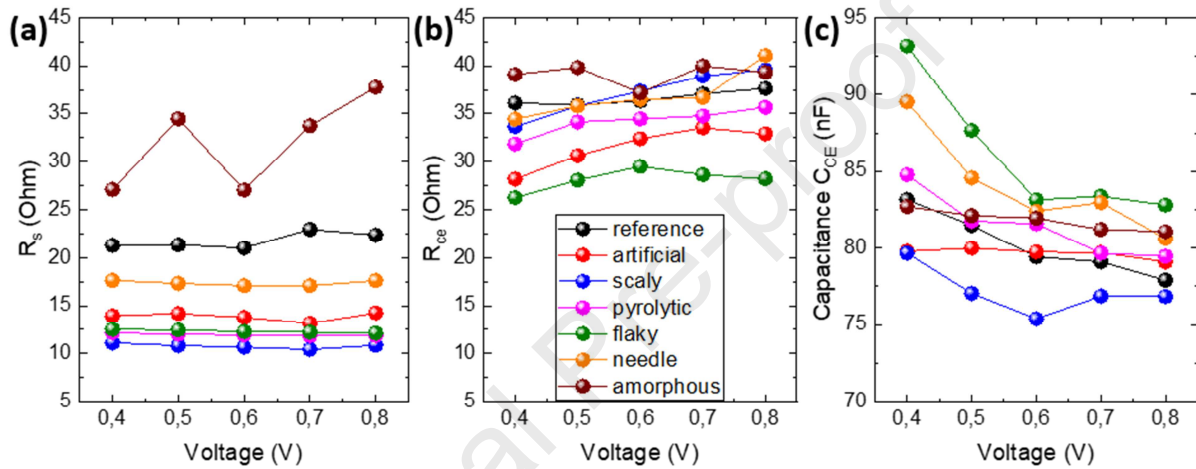

Figure 6: *R_s and R_{CE} extracted from the Nyquist plots at different applied voltage bias for C-PSCs with various graphite types*

Looking closer at the semi-circle corresponding to carbon/perovskite interface, it can be noticed that cells with reference, artificial and scaly graphites display the smallest capacitance at the interface with values below 80 nF (Fig. 6c). This means that less charge accumulation happens on each side of the interface, providing an easier hole injection from perovskite to carbon and resulting in higher J_{sc} values. To confirm this, we additionally perform time-resolved photoluminescence (TRPL) measurements, evaluating charge carrier extraction by the selective layers. The only difference between the samples is the graphite source, which makes it reasonable to assume that perovskite/m-TiO$_2$ interface is similar in all cases, as also suggested by the EIS results. Thus, it is reasonable to assume that the variations between the PL decays after excitation arises from the different graphite types and carbon/perovskite contact. The carrier extraction time was estimated by fitting the TRPL measurement to a bi-exponential decay function (Fig. S7). Scaly, artificial and reference graphites have a short extraction time of 6.92 ns, 9.79 ns and 10.54 ns respectively, whereas in cells with pyrolytic, flaky, needle and amorphous

graphite types, charge extraction time is longer – 14.91 ns, 22.63 ns, 12.37 ns and 11.53 ns respectively. The shorter charge carrier extraction time suggests that the hole extraction by graphite are enhanced, leading to higher photo-currents, which have been demonstrated earlier in Fig.4.

The difference in V_{oc} between cells with different graphites, suggests that the non-radiative recombination at the back-contact can also be influenced by the graphite type. The transient V_{oc} measurement conducted in high-perturbation mode (details in Experimental Section) are shown in Fig.S8 which indicates that the charge carrier recombination at the back-contact is slower in cells with scaly graphite, followed by reference, artificial and amorphous types. The fastest recombination seen in the V_{oc} decay occurs in cells with needle graphite, suggesting that the recombination at the perovskite/carbon interface in such type of cells is the highest. Interestingly, amorphous flakes, which have the highest portion of non-graphitic carbon (as was demonstrated from Raman Shift spectra) does not have a negative effect on the recombination at the back contact and V_{oc}. The trend between the recombination at the back-contact aligns with the measured V_{oc} obtained from the J-V scan of respective graphite types, where the scaly and amorphous graphites which have the highest V_{oc} exhibit longer charge carrier lifetime, whereas in flaky and needle types it is shorter resulting in a lower V_{oc}.
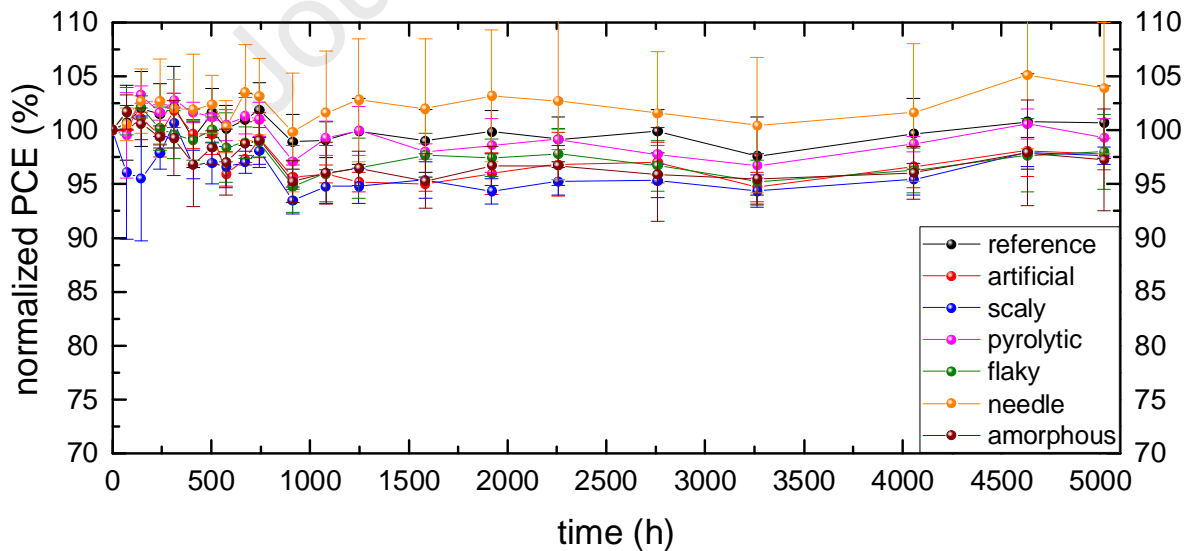

Figure 7: *PCE evolution during the storage of non-encapsulated C-PSCs under ambient environment (R.H. = 40 - 50%) in the dark. Each data point represents an average between the measured samples of each point with a std. deviation.*

As was shown earlier, the graphite type can also affect the carbon-layer morphology. HSL-free C-PSCs typically exhibit higher stability than cells with HSLs and metal-based contacts. Besides the fact that graphite itself does not degrade or react with the perovskite, this could be due to the presence thick hydrophobic carbon-based back-contact filled with perovskite that prevents moisture ingress. The latter implies that, thinner and less homogeneous carbon layers could facilitate easier moisture and air ingress into the sensitive perovskite photoabsorber, leading to faster degradation. In order to evaluate the effect of graphite type on cell's stability, cells with different graphite types were stored under ambient conditions (40-50% rel. humidity) in the dark for 5,000 hours. As seen from the Fig.7, the scaly and amorphous graphites show the fastest degradation, losing less than 3% of the initial efficiency, whereas the cells with needle and reference graphites demonstrate high shelf-stability by retaining nearly same PCE or even higher during the whole ageing period. Notably, the cells with pyrolytic graphite also appear to be more stable, which we attribute to the absence of voids in the carbon-based cathode, which appeared during the layer deposition. In contrast, C-PSCs with other graphite types have a slightly reduced performance that we attribute to an easier ingress of moisture and air into the sensitive perovskite photoabsrober, leading to degradation. Although the electrodes based on amorphous graphite were deposited homogeneously, the observed degradation is likely to be related to a small particle graphite size (as was seen from SEM images earlier), which cannot provide a sufficient protection against ambient environment. These results point out that in order to ensure the long-term stability of cells with carbon-based electrodes, the paste rheology, particle size and homogeneity of the deposition have to be carefully optimized.

4. Conclusion

In this work, we have analyzed the differences between three types of naturally-occurring graphites, namely, scaly, flaky and amorphous, as well as three types of synthetic graphites: artificial fine powder graphite, highly ordered pyrolytic one and needle graphite in the context of applications for carbon-based electrodes for perovskite solar cells. We compared their properties with our reference graphite – Elocarb B/SP, obtained from Solaronix S.A. The scaly type, having a unique graphitization route, yielded graphite particles with the largest crystallite dimensions, whereas pyrolytic graphite had the lowest number of structural defects. The FF of the fabricated cells was found to be most affected by different graphite types and is influenced not only by

sheet resistance of the electrodes, but also by its interfacial resistance to perovskite. The electrodes produced from the pyrolytic, flaky and scaly graphite had the least series resistance losses, leading to FFs above 70% in cells with a 0.64 cm^2 active area. Although the cells with pyrolytic graphite exhibited the least series resistance loss, the J_{sc} of these cells were reduced due to the build-up of a higher capacitance and reduced charge extraction at perovskite/carbon interface. Interestingly, under continuous sun illumination, the overall difference in V_{oc} for cells with all graphite types is rather low – approximately 50 mV. C-PSCs with electrodes made from scaly and artificial graphites has proven to have better charge transport properties, resulting in enhanced photovoltaic performance, where the champion cell with a scaly graphite reached a PCE of 14.6 %. The printability and adhesion to the layer underneath was found to affect the homogeneity of the electrode deposition, which was found to affect the cell moisture-stability. All the C-PSCs were found to be quite stable, where the least stable cells with scaly and amorphous graphite lost less than 3% of initial PCE after 5,000 h of storage in the ambient environment. The reference cells with electrodes based on Elocarb B/SP paste remained the initial PCE, while the cells with needle-based graphite had slightly improved performance after ageing. This work paves a way towards optimizing the low-cost and up-scalable carbon-based electrodes for efficient perovskite PV devices with low series resistance losses, which is essential for its successful commercialization.

Conflicts of interest

There are no conflicts to declare.

Acknowledgements

References

(1) Dunlap-Shohl, W. A.; Zhou, Y.; Padture, N. P.; Mitzi, D. B. Synthetic Approaches for Halide Perovskite Thin Films. *Chemical reviews* **2019**, *119* (5), 3193–3295. DOI: 10.1021/acs.chemrev.8b00318.

(2) Egger, D. A.; Bera, A.; Cahen, D.; Hodes, G.; Kirchartz, T.; Kronik, L.; Lovrincic, R.; Rappe, A. M.; Reichman, D. R.; Yaffe, O. What Remains Unexplained about the Properties of Halide Perovskites? *Advanced materials (Deerfield Beach, Fla.)* **2018**, *30* (20), e1800691. DOI: 10.1002/adma.201800691.

(3) NREL. *Best Research-Cell Efficiency Chart*. https://www.nrel.gov/pv/cell-efficiency.html.

(4) Rong, Y.; Hu, Y.; Mei, A.; Tan, H.; Saidaminov, M. I.; Seok, S. I.; McGehee, M. D.; Sargent, E. H.; Han, H. Challenges for commercializing perovskite solar cells. *Science (New York, N.Y.)* **2018**, *361* (6408). DOI: 10.1126/science.aat8235.

(5) Li, Z.; Klein, T. R.; Kim, D. H.; Yang, M.; Berry, J. J.; van Hest, M. F. A. M.; Zhu, K. Scalable fabrication of perovskite solar cells. *Nat Rev Mater* **2018**, *3* (4). DOI: 10.1038/natrevmats.2018.17.

(6) Ku, Z.; Rong, Y.; Xu, M.; Liu, T.; Han, H. Full printable processed mesoscopic CH☐NH☐PbI☐/TiO☐ heterojunction solar cells with carbon counter electrode. *Scientific reports* **2013**, *3*, 3132. DOI: 10.1038/srep03132.

(7) Hu, Y.; Si, S.; Mei, A.; Rong, Y.; Liu, H.; Li, X.; Han, H. Stable Large-Area (10 × 10 cm 2) Printable Mesoscopic Perovskite Module Exceeding 10% Efficiency. *Sol. RRL* **2017**, *1* (2), 1600019. DOI: 10.1002/solr.201600019.

(8) Gong, J.; Darling, S. B.; You, F. Perovskite photovoltaics: life-cycle assessment of energy and environmental impacts. *Energy Environ. Sci.* **2015**, *8* (7), 1953–1968. DOI: 10.1039/C5EE00615E.

(9) Domanski, K.; Correa-Baena, J.-P.; Mine, N.; Nazeeruddin, M. K.; Abate, A.; Saliba, M.; Tress, W.; Hagfeldt, A.; Grätzel, M. Not All That Glitters Is Gold: Metal-Migration-Induced Degradation in Perovskite Solar Cells. *ACS Nano* **2016**, *10* (6), 6306–6314. DOI: 10.1021/acsnano.6b02613.

(10) Wang, Q.; Phung, N.; Di Girolamo, D.; Vivo, P.; Abate, A. Enhancement in lifespan of halide perovskite solar cells. *Energy Environ. Sci.* **2019**, *12* (3), 865–886. DOI: 10.1039/C8EE02852D.

(11) Svanström, S.; Jacobsson, T. J.; Boschloo, G.; Johansson, E. M. J.; Rensmo, H.; Cappel, U. B. Degradation Mechanism of Silver Metal Deposited on Lead Halide Perovskites. *ACS applied materials & interfaces* **2020**, *12* (6), 7212–7221. DOI: 10.1021/acsami.9b20315.

(12) Hawash, Z.; Ono, L. K.; Raga, S. R.; Lee, M. V.; Qi, Y. Air-Exposure Induced Dopant Redistribution and Energy Level Shifts in Spin-Coated Spiro-MeOTAD Films. *Chem. Mater.* **2015**, *27* (2), 562–569. DOI: 10.1021/cm504022q.

(13) Wagner, L.; Mastroianni, S.; Hinsch, A. Reverse Manufacturing Enables Perovskite Photovoltaics to Reach the Carbon Footprint Limit of a Glass Substrate. Joule, 4(4), 882-901 **2020.** DOI: 10.1016/J.JOULE.2020.02.001.

(14) Meng, F.; Liu, A.; Gao, L.; Cao, J.; Yan, Y.; Wang, N.; Fan, M.; Wei, G.; Ma, T. Current progress in interfacial engineering of carbon-based perovskite solar cells. *J. Mater. Chem. A* **2019**, *7* (15), 8690–8699. DOI: 10.1039/C9TA01364D.

 (15) Fagiolari, L.; Bella, F. Carbon-based materials for stable, cheaper and large-scale processable perovskite solar cells. *Energy Environ. Sci.* **2019**, *12* (12), 3437–3472. DOI: 10.1039/C9EE02115A.

 (16) Hadadian, M.; Smått, J.-H.; Correa-Baena, J.-P. The role of carbon-based materials in enhancing the stability of perovskite solar cells. *Energy Environ. Sci.* **2020**, *13* (5), 1377–1407. DOI: 10.1039/C9EE04030G.

 (17) Chen, J.; Xiong, Y.; Rong, Y.; Mei, A.; Sheng, Y.; Jiang, P.; Hu, Y.; Li, X.; Han, H. Solvent effect on the hole-conductor-free fully printable perovskite solar cells. *Nano Energy* **2016**, *27*, 130–137. DOI: 10.1016/j.nanoen.2016.06.047.

 (18) Zhou, H.; Shi, Y.; Dong, Q.; Zhang, H.; Xing, Y.; Wang, K.; Du, Y.; Ma, T. Hole-Conductor-Free, Metal-Electrode-Free TiO2/CH3NH3PbI3 Heterojunction Solar Cells Based on a Low-Temperature Carbon Electrode. *The journal of physical chemistry letters* **2014**, *5* (18), 3241–3246. DOI: 10.1021/jz5017069.

 (19) Mei, A.; Li, X.; Liu, L.; Ku, Z.; Liu, T.; Rong, Y.; Xu, M.; Hu, M.; Chen, J.; Yang, Y.; Grätzel, M.; Han, H. A hole-conductor-free, fully printable mesoscopic perovskite solar cell with high stability. *Science (New York, N.Y.)* **2014**, *345* (6194), 295–298. DOI: 10.1126/science.1254763.

 (20) Mathiazhagan, G.; Wagner, L.; Bogati, S.; Ünal, K. Y.; Bogachuk, D.; Kroyer, T.; Mastroianni, S.; Hinsch, A. Double-Mesoscopic Hole-Transport-Material-Free Perovskite Solar Cells: Overcoming Charge-Transport Limitation by Sputtered Ultrathin Al2O3 Isolating Layer. *ACS applied nano materials* **2020**, *3* (3), 2463–2471. DOI: 10.1021/acsanm.9b02563.

 (21) Hashmi, S. G.; Martineau, D.; Li, X.; Ozkan, M.; Tiihonen, A.; Dar, M. I.; Sarikka, T.; Zakeeruddin, S. M.; Paltakari, J.; Lund, P. D.; Grätzel, M. Air Processed Inkjet Infiltrated Carbon Based Printed Perovskite Solar Cells with High Stability and Reproducibility. *Adv. Mater. Technol.* **2017**, *2* (1), 1600183. DOI: 10.1002/admt.201600183.

 (22) Dmitry Bogachuk; Salma Zouhair; Konrad Wojciechowski; Bowen Yang; Vivek Babu; Lukas Wagner; Bo Xu; Jaekeun Lim; Simone Mastroianni; Henrik Pettersson; Anders Hagfeldt; Andreas Hinsch. Low-temperature carbon-based electrodes in perovskite solar cells. *Energy Environ. Sci.* **2020.** DOI: 10.1039/D0EE02175J.

 (23) Chung, D. D. L. *Journal of Materials Science* **2002**, *37* (8), 1475–1489. DOI: 10.1023/A:1014915307738.

 (24) Wissler, M. Graphite and carbon powders for electrochemical applications. *Journal of Power Sources* **2006**, *156* (2), 142–150. DOI: 10.1016/j.jpowsour.2006.02.064.

 (25) Hashmi, S. G.; Martineau, D.; Dar, M. I.; Myllymäki, T. T. T.; Sarikka, T.; Ulla, V.; Zakeeruddin, S. M.; Grätzel, M. High performance carbon-based printed perovskite solar cells with humidity assisted thermal treatment. *J. Mater. Chem. A* **2017**, *5* (24), 12060–12067. DOI: 10.1039/C7TA04132B.

 (26) Duan, M.; Tian, C.; Hu, Y.; Mei, A.; Rong, Y.; Xiong, Y.; Xu, M.; Sheng, Y.; Jiang, P.; Hou, X.; Zhu, X.; Qin, F.; Han, H. Boron-Doped Graphite for High Work Function Carbon Electrode in Printable Hole-Conductor-Free Mesoscopic Perovskite Solar Cells. *ACS applied materials & interfaces* **2017**, *9* (37), 31721–31727. DOI: 10.1021/acsami.7b05689.

(27) Grancini, G.; Roldán-Carmona, C.; Zimmermann, I.; Mosconi, E.; Lee, X.; Martineau, D.; Narbey, S.; Oswald, F.; Angelis, F. de; Graetzel, M.; Nazeeruddin, M. K. One-Year stable perovskite solar cells by 2D/3D interface engineering. *Nature communications* **2017**, *8*, 15684. DOI: 10.1038/ncomms15684.

(28) Mishra, A.; Ahmad, Z.; Zimmermann, I.; Martineau, D.; Shakoor, R. A.; Touati, F.; Riaz, K.; Al-Muhtaseb, S. A.; Nazeeruddin, M. K. Effect of annealing temperature on the performance of printable carbon electrodes for perovskite solar cells. *Organic Electronics* **2019**, *65*, 375–380. DOI: 10.1016/j.orgel.2018.11.046.

(29) Verma, A.; Martineau, D.; Hack, E.; Makha, M.; Turner, E.; Nüesch, F.; Heier, J. Towards industrialization of perovskite solar cells using slot die coating. *J. Mater. Chem. C* **2020**, *8* (18), 6124–6135. DOI: 10.1039/D0TC00327A.

(30) Dasgupta, K.; Sathiyamoorthy, D. Disordered carbon–its preparation, structure, and characterisation. *Materials Science and Technology* **2003**, *19* (8), 995–1002. DOI: 10.1179/026708303225004693.

(31) Meng, J.; Li, S.; Niu, J. Crystallite Structure Characteristics and Its Influence on Methane Adsorption for Different Rank Coals. *ACS omega* **2019**, *4* (24), 20762–20772. DOI: 10.1021/acsomega.9b03165.

(32) E. Crespo; F. J. Luque; J. F. Barrenechea; M. Rodas. Influence of grinding on graphite crystallinity from experimental and natural data: implications for graphite thermometry and sample preparation. *Mineralogical Magazine* **2006**, *70* (6), 697–707. DOI: 10.1180/0026461067060358.

(33) Warren, B. E. X-Ray Diffraction in Random Layer Lattices. *Phys. Rev.* **1941**, *59* (9), 693–698. DOI: 10.1103/PhysRev.59.693.

(34) Schuepfer, D. B.; Badaczewski, F.; Guerra-Castro, J. M.; Hofmann, D. M.; Heiliger, C.; Smarsly, B.; Klar, P. J. Assessing the structural properties of graphitic and non-graphitic carbons by Raman spectroscopy. *Carbon* **2020**, *161*, 359–372. DOI: 10.1016/j.carbon.2019.12.094.

(35) Peng, W.; Li, H.; Hu, Y.; Liu, Y.; Song, S. Characterisation of reduced graphene oxides prepared from natural flaky, lump and amorphous graphites. *Materials Research Bulletin* **2016**, *78*, 119–127. DOI: 10.1016/j.materresbull.2016.02.034.

(36) Ohler, M.; Baruchel, J.; Moore, A. W.; Galez, P.; Freund, A. Direct observation of mosaic blocks in highly oriented pyrolytic graphite. *Nuclear Instruments and Methods in Physics Research Section B: Beam Interactions with Materials and Atoms* **1997**, *129* (2), 257–260. DOI: 10.1016/S0168-583X(97)00204-8.

(37) Amirah Way; Joel Luke; Alex D. Evans; Zhe Li; Ji-Seon Kim; James R. Durrant; Harrison Ka Hin Lee; Wing C. Tsoi. Fluorine doped tin oxide as an alternative of indium tin oxide for bottom electrode of semi-transparent organic photovoltaic devices. *AIP Advances* **2019**, *9* (8), 85220. DOI: 10.1063/1.5104333.

(38) Sima, C.; Grigoriu, C.; Antohe, S. Comparison of the dye-sensitized solar cells performances based on transparent conductive ITO and FTO. *Thin Solid Films* **2010**, *519* (2), 595–597. DOI: 10.1016/j.tsf.2010.07.002.

(39) Lucera, L.; Machui, F.; Kubis, P.; Schmidt, H. D.; Adams, J.; Strohm, S.; Ahmad, T.; Forberich, K.; Egelhaaf, H.-J.; Brabec, C. J. Highly efficient, large area, roll coated flexible and rigid OPV modules with

geometric fill factors up to 98.5% processed with commercially available materials. Energy & Environmental Science, 9(1), 89-94 **2016.** DOI: 10.1039/C5EE03315B.

Graphical Abstract
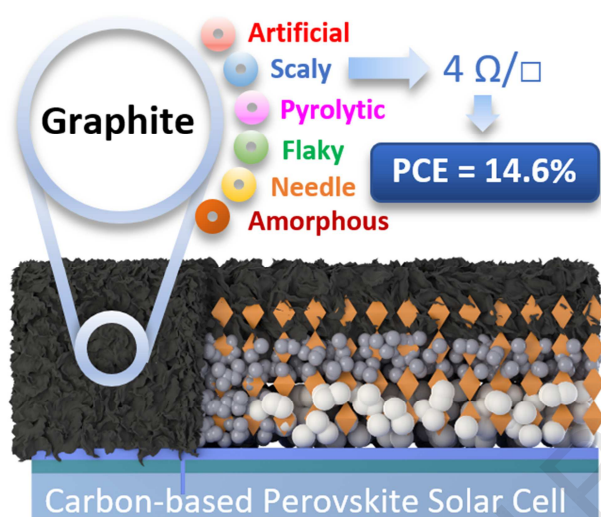
Declaration of interests

☒ The authors declare that they have no known competing financial interests or personal relationships that could have appeared to influence the work reported in this paper.

☐The authors declare the following financial interests/personal relationships which may be considered as potential competing interests: